

## MIT Open Access Articles

*Current dark matter annihilation  
constraints from CMB and low-redshift data*

The MIT Faculty has made this article openly available. **Please share** how this access benefits you. Your story matters.

**Citation:** Madhavacheril, Mathew S., Neelima Sehgal, and Tracy R. Slatyer. "Current Dark Matter Annihilation Constraints from CMB and Low-Redshift Data." Phys. Rev. D 89, no. 10 (May 2014). © 2014 American Physical Society

**As Published:** <http://dx.doi.org/10.1103/PhysRevD.89.103508>

**Publisher:** American Physical Society

**Persistent URL:** <http://hdl.handle.net/1721.1/88661>

**Version:** Final published version: final published article, as it appeared in a journal, conference proceedings, or other formally published context

**Terms of Use:** Article is made available in accordance with the publisher's policy and may be subject to US copyright law. Please refer to the publisher's site for terms of use.



# Current dark matter annihilation constraints from CMB and low-redshift data

Mathew S. Madhavacheril,<sup>1</sup> Neelima Sehgal,<sup>1</sup> and Tracy R. Slatyer<sup>2</sup>

<sup>1</sup>*Stony Brook University, Stony Brook, New York 11794, USA*

<sup>2</sup>*Massachusetts Institute of Technology, Cambridge, Massachusetts 02139, USA*

(Received 15 October 2013; published 7 May 2014)

Updated constraints on the dark matter cross section and mass are presented combining cosmic microwave background (CMB) power spectrum measurements from Planck, WMAP9, ACT, and SPT as well as several low-redshift data sets (BAO, HST, and supernovae). For the CMB data sets, we combine WMAP9 temperature and polarization data for  $l \leq 431$  with Planck temperature data for  $432 \leq l \leq 2500$ , ACT and SPT data for  $l > 2500$ , and Planck CMB four-point lensing measurements. We allow for redshift-dependent energy deposition from dark matter annihilation by using a “universal” energy absorption curve. We also include an updated treatment of the excitation, heating, and ionization energy fractions and provide an updated deposition efficiency factors ( $f_{\text{eff}}$ ) for 41 different dark matter models. Assuming perfect energy deposition ( $f_{\text{eff}} = 1$ ) and a thermal cross section, dark matter masses below 26 GeV are excluded at the  $2\sigma$  level. Assuming a more generic efficiency of  $f_{\text{eff}} = 0.2$ , thermal dark matter masses below 5 GeV are disfavored at the  $2\sigma$  level. These limits are a factor of  $\sim 2$  improvement over those from WMAP9 data alone. These current constraints probe, but do not exclude, dark matter as an explanation for reported anomalous indirect detection observations from AMS-02/PAMELA and the Fermi gamma-ray inner-Galaxy data. They also probe relevant models that would explain anomalous direct detection events from CDMS, CRESST, CoGeNT, and DAMA, as originating from a generic thermal weakly interacting massive particle. Projected constraints from the full Planck release should improve the current limits by another factor of  $\sim 2$  but will not definitely probe these signals. The proposed CMB Stage IV experiment will more decisively explore the relevant regions and improve upon the Planck constraints by another factor of  $\sim 2$ .

DOI: [10.1103/PhysRevD.89.103508](https://doi.org/10.1103/PhysRevD.89.103508)

PACS numbers: 95.35.+d, 98.80.-k

## I. INTRODUCTION

Nonbaryonic matter is a crucial ingredient in our current understanding of the cosmological history of the Universe. A significant fraction of the energy density of the Universe is contended to consist of “dark matter” that interacts only very weakly (if at all) with ordinary matter. Dark matter is needed to explain numerous observations including gravitational lensing by clusters and galaxies, galaxy rotation curves, acoustic peaks in the power spectrum of the cosmic microwave background (CMB), and the growth of large-scale structure. However, all of the widely accepted evidence for dark matter is sensitive only to its gravitational effects, and the determination of its particle nature is an important open problem. Current efforts to address this can broadly be divided into (i) indirect detection experiments that aim to detect the products of dark matter annihilation or decay, (ii) direct detection experiments that attempt to detect dark matter particles via their recoil off heavy nuclei, and (iii) collider experiments where dark matter particles are hoped to be identified in the products of high-energy collisions.

One particular indirect detection method is to observe the effect of dark matter annihilation early in the history of the Universe ( $1400 > z > 100$ ) on the CMB temperature and polarization anisotropies [1–11]. If dark matter particles

self-annihilate at a sufficient rate, the expected signal would be directly sensitive to the thermally averaged cross section  $\langle \sigma v \rangle$  of the dark matter particles in this epoch, the mass  $M_\chi$  of the annihilating particle, and the particular annihilation channel. An advantage of this indirect detection method over more local probes is that it is free of astrophysical uncertainties such as the local dark matter distribution and the astrophysical background of high-energy particles. In Sec. II, we review the physics behind the modification of the CMB power spectra by annihilating dark matter. We also discuss the universal energy deposition curve and systematic corrections to it as in Ref. [8] and the leverage in multipole space of the dark matter constraints. Updated constraints including all available data are presented in Sec. III. In Sec. IV, we discuss these results in light of recent data from other indirect and direct dark matter searches.

## II. EFFECT OF DARK MATTER ANNIHILATION ON THE CMB

The recombination history of the Universe could potentially be modified by dark matter particles annihilating into Standard Model particles, which in turn inject energy into the (pre-recombination) photon-baryon plasma and (post-recombination) gas and background radiation. Previous

authors [1–5] have considered the effects of this energy injection, which broadly consist of (i) increased ionization of the gas, (ii) atomic excitation of the gas, and (iii) plasma/gas heating. These processes in turn lead to an increase in the residual ionization fraction ( $x_e$ ) and baryon temperature ( $T_b$ ) after recombination. For rates of energy injection low enough that there is minimal shift in the positions of the first few peaks of the CMB temperature power spectrum, the primary effect of the energy injection is to broaden the surface of last scattering. This leads to an attenuation of the temperature and polarization power spectra that is most pronounced at small scales. In addition, the positions of the temperature-polarization (TE) and polarization (EE) peaks shift and the power of polarization fluctuations at large scales ( $l < 500$ ) increases as the thickness of the last scattering surface grows. (See Fig. 4 in Ref. [1] for a depiction of this effect.)

The rate of energy deposition per volume is given by

$$\frac{dE}{dVdt} = \rho_c^2 c^2 \Omega_{\text{DM}}^2 (1+z)^6 p_{\text{ann}}(z) \quad (1)$$

$$p_{\text{ann}}(z) = f(z) \frac{\langle \sigma v \rangle}{M_\chi}, \quad (2)$$

where  $\rho_c$  is the critical density of the Universe today,  $\Omega_{\text{DM}}$  is the density of cold dark matter today,  $\langle \sigma v \rangle$  is the thermally averaged cross section of self-annihilating dark matter,  $M_\chi$  is the dark matter mass, and  $f(z)$  is an  $\mathcal{O}(1)$  redshift-dependent function that describes the fraction of energy that is absorbed by the CMB plasma. In this parametrization,  $f(z)$  captures the redshift dependence of the energy deposition not included in the  $(1+z)^3$  evolution of the dark matter density. The exact functional form of  $f(z)$  depends on the specific annihilation channel of dark matter; however, as discussed in Ref. [5] and in Sec. II A, the first principal component formed from the  $f(z)$  energy deposition curves of 41 representative dark matter models accounts for more than 99.9% of the variance in the CMB power spectra that is not degenerate with other standard cosmological parameters. The injected energy modifies the evolution of the ionization fraction,  $x_e$ , according to

$$\frac{dx_e}{dz} = \frac{1}{(1+z)H(z)} [R_s(z) - I_s(z) - I_X(z)], \quad (3)$$

where  $R_s(z)$  and  $I_s(z)$  are the standard recombination and ionization rates, respectively, in the absence of dark matter annihilation,  $I_X(z)$  is the modification to ionization due to dark matter annihilation, and  $H(z)$  is the Hubble constant at redshift  $z$ . Standard recombination, as discussed in Ref. [12], is described by

$$[R_s(z) - I_s(z)] = C \times [x_e^2 n_H \alpha_B - \beta_B (1 - x_e) e^{-h\nu_{2s}/k_B T_b}], \quad (4)$$

where the  $C$  factor is given by

$$C = \frac{[1 + K\Lambda_{2s1s}n_H(1-x_e)]}{[1 + K\Lambda_{2s1s}n_H(1-x_e) + K\beta_B n_H(1-x_e)]}. \quad (5)$$

Here,  $n_H$  is the hydrogen number density;  $T_b$  is the baryon gas temperature;  $\alpha_B$  and  $\beta_B$  are the effective recombination and photoionization rates, respectively, for  $n \geq 2$ ;  $\nu_{2s}$  is the change in frequency from the  $2s$  level to the ground state;  $\Lambda_{2s1s}$  is the decay rate of the metastable  $2s$  level to  $1s$ ;  $K = \lambda_\alpha^3 / (8\pi H(z))$ ; and  $\lambda_\alpha$  is the wavelength of the Lyman- $\alpha$  transition from  $n=2$  to  $n=1$ . This  $C$  factor is approximately the probability that a hydrogen atom in the excited  $n=2$  state will decay by two-photon emission to the  $n=1$  state before being photodissociated [12].

Several authors have considered adding generic terms to the recombination equations, denoted by

$$I_X(z) = I_{X_i}(z) + I_{X_\alpha}(z), \quad (6)$$

that account for additional ionization from the ground state and from the  $n=2$  state after energy injection [2,13,14]. Dark matter annihilation increases the ionization fraction through (i) direct ionization of hydrogen atoms from the ground state [ $I_{X_i}(z)$ ] and (ii) ionization from the  $n=2$  state after hydrogen has been excited by Lyman- $\alpha$  photons produced by dark matter annihilation [ $I_{X_\alpha}(z)$ ]. Following Ref. [4], the rate of additional ionization from the ground state is given by

$$I_{X_i} = \chi_i \frac{[dE/dVdt]}{n_H(z)E_i}, \quad (7)$$

where  $E_i$  is the average ionization energy per baryon (13.6 eV) and  $\chi_i$  is the fraction of absorbed energy that goes directly into ionization.

The term describing ionization from the  $n=2$  state is given by

$$I_{X_\alpha} = (1-C)\chi_\alpha \frac{[dE/dVdt]}{n_H(z)E_\alpha}, \quad (8)$$

where  $\chi_\alpha$  is the fraction of absorbed energy that goes into excitation,  $E_\alpha$  is the difference in binding energy between the  $n=1$  and  $n=2$  levels (10.2 eV), and  $(1-C)$  is the probability of not decaying to the  $n=1$  state before being photoionized from the  $n=2$  state.

In addition, the baryon temperature evolution is modified by the last term in

$$(1+z) \frac{dT_b}{dz} = \frac{8\sigma_T a_R T_{\text{CMB}}^4}{3m_e c H(z)} \frac{x_e}{1 + f_{\text{He}} + x_e} (T_b - T_{\text{CMB}}) + 2T_b - \frac{2}{3k_B H(z)} \frac{K_h}{1 + f_{\text{He}} + x_e}, \quad (9)$$

where  $f_{\text{He}}$  is the Helium fraction and

$$K_h = \chi_h \frac{[dE/dVdt]}{n_H(z)}. \quad (10)$$

Here,  $\chi_h$  is the absorbed energy converted to heat. The energy fractions ( $\chi_i, \chi_\alpha$ , and  $\chi_h$ ) are discussed further in Sec. II A.

### A. Universal energy deposition curve with systematic corrections

Many earlier studies of the impact of dark matter (DM) annihilation on recombination (e.g., Refs. [1,2,4,5,9,11,15–17]) used an approximate form for the energy fractions  $\chi_i, \chi_\alpha$ , and  $\chi_h$ , derived from Monte Carlo studies by Shull and van Steenberg in 1985 [18] and following the approximate fit suggested in Ref. [19]:

$$\begin{aligned} \chi_i &= \chi_e = \frac{(1 - x_H)}{3} \\ \chi_h &= \frac{1 + 2x_H + f_{\text{He}}(1 + 2x_{\text{He}})}{3(1 + f_{\text{He}})}. \end{aligned} \quad (11)$$

Here,  $\chi_i$  is the hydrogen ionization fraction,  $\chi_e$  is the hydrogen excitation fraction, and  $\chi_h$  is the heating fraction. The Lyman- $\alpha$  contribution,  $\chi_\alpha$ , is some fraction of  $\chi_e$ . Some past studies have taken  $\chi_\alpha = 0$  to obtain conservative constraints, while others, including this work, set  $\chi_\alpha = \chi_e$ . The helium fraction  $f_{\text{He}}$  is given by  $f_{\text{He}} = Y_p / (4(1 - Y_p))$ , where  $Y_p$  is the helium mass fraction. The ratio of ionized hydrogen to total hydrogen is given by  $x_H$ , and the ratio of ionized helium to total helium is given by  $x_{\text{He}}$ . In this work, we do not include ionization of helium due to dark matter annihilations since it has a negligible impact on the CMB power spectra [8,17].

In reality, the dependence of the energy fractions on the background ionization fraction  $x_H$  is more complex than the simple linear dependence in Eq. (11). The energy fractions also possess a nontrivial dependence on the energy of the electron when it is “deposited” to the plasma (i.e., when its energy drops to the point where all subsequent cooling processes have time scales much faster than a Hubble time). In previous work (e.g., Ref. [3]), deposited photons with energies above 13.6 eV were treated exactly as deposited electrons, under the presumption that such photons would quickly ionize the gas, producing a free electron. While this is true, it is important to also account for the energy absorbed in the ionization itself. The free electron produced by photoionization will then deposit its energy subject to the appropriate energy fractions.

In this work we take these effects into account following the method described in detail in Ref. [8]; our results use the same set of assumptions as that paper’s “best estimate” constraints. Electrons, positrons, and photons injected by DM annihilation are tracked down to a deposition scale of

3 keV, taking the expansion of the Universe into account, using an improved version of the code first described in Ref. [3]. The spectra of photons and electrons below this energy are stored—many of the energy-loss processes are discrete rather than continuous, and thus these spectra are not simply spikes at the deposition scale—and then integrated over energy-dependent energy loss fractions computed by Monte Carlo methods, following Refs. [20–23]. This part of the code does not take redshifting into account, but at energies below 3 keV, all cooling times are much faster than a Hubble time (with the notable exception of photons below 10.2 eV after the redshift of last scattering), so the expansion can be neglected. Energy losses to direct ionization, excitation, and heating by electrons and photons above the 3 keV threshold are calculated in the “high-energy” code (appropriate to energies above 3 keV) and added to the corresponding fractions. “Continuum” (below 10.2 eV) and Lyman- $\alpha$  photons produced by inverse Compton scattering (ICS) of electrons above 3 keV are likewise calculated in the high-energy code; for electrons below 3 keV, ICS quickly becomes subdominant to atomic energy loss processes. Ionizations on helium are taken into account following Ref. [8].

The primary difference between the results of this method and earlier approximations is that the correct treatment of ICS by nonrelativistic electrons predicts greater energy transfer into continuum photons, which cannot subsequently induce ionizations or Lyman- $\alpha$  excitations; the effect can be regarded as a high-energy distortion to the CMB energy spectrum. Consequently, the fraction of power going into ionization, excitation, and heating of the gas is somewhat depressed. There is an exception at high redshifts, where accounting for the additional ionization from *photon*-gas interactions (which was not done in, e.g., Ref. [3], which treated low-energy electrons and photons as identical) can outweigh the reduced ionization from electron-gas interactions, since the latter is very small in any treatment (those electrons lose their energy dominantly to Coulomb heating, using either the approximate fractions or the more accurate ones).

We have computed the fraction of deposited energy going into ionization,  $\chi_i$ , which largely controls the constraints (the Lyman- $\alpha$  fraction,  $\chi_\alpha$ , has a small, albeit not negligible, effect [8]), as a function of redshift, for each of the 41 annihilation channels described in Ref. [3]. The calculations of the energy fractions in Ref. [8] separately compute the ionization on helium; here, we simply sum the total power into ionization on hydrogen and helium to obtain the  $\chi_i$  fraction, since, as mentioned previously, the effects of separating the helium fraction are small. For convenience, given the widespread use of the approximate fractions of Eq. (11) in the literature and in existing code, for each annihilation channel, we can define a new “effective  $f(z)$  curve”,  $f_{\text{sys}}(z)$ , which yields the correct



power into ionization when multiplied by the *approximate* value of  $\chi_i$ . That is,

$$\chi_i^{\text{approx}}(z)f_{\text{sys}}(z) = \chi_i^{\text{updated}}(z)f_{\text{old}}(z), \quad (12)$$

where  $\chi_i^{\text{approx}}$  and  $\chi_i^{\text{updated}}$  are, respectively, the approximate [Eq. (11)] and updated (following Ref. [8]) energy fractions and  $f_{\text{old}}(z)$  agrees with the results of Ref. [3]. [Note that in some cases this definition can lead to a very large value of  $f_{\text{sys}}(z)$ , much greater than 1, where  $\chi_i^{\text{approx}}(z) \ll \chi_i^{\text{updated}}(z)$ .] This curve should not generally be applied to compute the heating and Lyman- $\alpha$  components in cases where they are important; it is designed to correctly normalize the power into ionization. However, since we expect the effect of additional ionizations to dominate over the modification due to excitations or heating, we use the same  $f_{\text{sys}}(z)$  curve for the ionization, excitation, and heating terms. We checked that using the  $f_{\text{sys}}(z)$  curve to multiply the ionization term and the old  $f(z)$  curve for the excitation and heating terms makes no appreciable difference to the constraints obtained below.

Having derived new individual  $f_{\text{sys}}(z)$  curves for a range of Standard Model final states, we can perform a principal component analysis using these curves as basis vectors, as described in detail in Ref. [5]. The first principal component describes the direction in this space [of linear combinations of the  $f_{\text{sys}}(z)$  curves], which captures the greatest amount of the variance in the CMB power spectra—in this case, over 99.9%. Physically, the effects of the different annihilation channels on the CMB anisotropy spectra are very similar.

We show in Fig. 1 the resulting first principal component as a function of redshift, which we refer to as the “universal”  $e(z)$  curve. The overall normalization of the

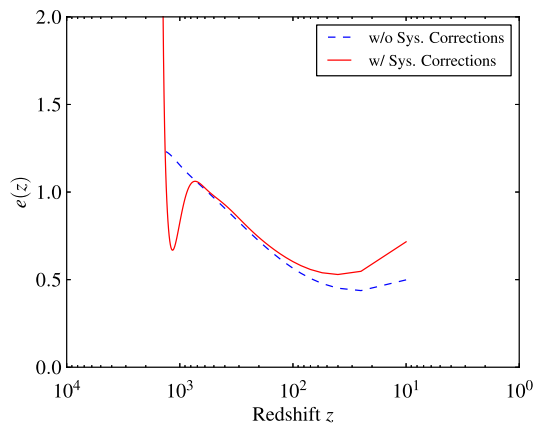


FIG. 1 (color online). Universal energy deposition curve,  $e(z)$ , using approximations for the fraction of energy converted to heat, ionization, and excitation (dashed blue curve), and accounting for more accurate calculations of the energy fractions from Ref. [8] (solid red curve).

curve is arbitrary since it is precisely its amplitude that we wish to constrain, and hence a rescaling of  $e(z)$  would be reflected in a proportional rescaling of the derived constraint on its coefficient. To fix the normalization, we adopt the convention used in Ref. [5]; i.e., we fix the normalization such that if  $p_{\text{ann}}(z) = \epsilon e(z)$  the Fisher matrix constraint on  $\epsilon$  is the same as that obtained for constant annihilation,  $p_{\text{ann}} = \epsilon$  (with approximate energy fractions), for some choice of experimental parameters. The advantage of this choice is that constraints on the coefficient of  $e(z)$  can be directly compared to previously derived constraints using constant  $p_{\text{ann}}$ . In this work, the Fisher matrix computation and principal component analysis were performed for a Planck-like experiment in the range  $\ell < 6000$ ; we have verified that performing the analysis instead for a cosmic variance limited experiment in this  $\ell$  range changes the shape and normalization of the  $e(z)$  curve only at the subpercent level. The principal components do not change appreciably when additional cosmological parameters that could be degenerate with the annihilation parameter are added. This is discussed in Appendix A5 of Ref. [5].

Note that this choice of normalization means that the  $e(z)$  curve does not reflect the general reduction in amplitude of the  $f_{\text{sys}}(z)$  curves relative to the older  $f(z)$  curves, arising from the fact that  $\chi_i^{\text{updated}}(z)$  is generally lower than  $\chi_i^{\text{approx}}(z)$ . To the degree that the Fisher matrix approach is valid, we expect the constraint on the coefficient of the updated  $e(z)$  curve to be identical to the corresponding bound for the older  $e(z)$  curve presented in Ref. [5], since both should be equivalent to the constraint using constant  $p_{\text{ann}}$  and approximate energy fractions. However, constraints on specific *models* will change.

To translate from constraints on the coefficient of the  $e(z)$  curve to constraints on a specific model, one must extract the coefficient of the first principal component, when the  $f_{\text{sys}}(z)$  curve for that model is expanded in the basis of principal components. This is referred to in Refs. [5] and [24] as taking a “dot product,” but there is a subtlety here in that the dot product must be taken in the space defined by the 41  $f_{\text{sys}}(z)$  curves, not in the space of functions of  $z$ . In the Fisher matrix approach, this corresponds to taking the dot product between the (discretized)  $f_{\text{sys}}(z)$  curve for that particular model and the vector  $(e)^T F$ , where  $e$  is the (discretized) universal  $e(z)$  curve and  $F$  is the marginalized Fisher matrix describing the effect on the CMB of energy depositions localized in redshift (see Ref. [5] for the precise construction). The dot product is normalized by dividing by the result where  $f_{\text{sys}}(z)$  is replaced with  $e(z)$ , to obtain an “effective  $f$ ” value  $f_{\text{eff,new}}$ :

$$f_{\text{eff,new}} = \frac{e(z) \cdot F \cdot f_{\text{sys}}(z)}{e(z) \cdot F \cdot e(z)}. \quad (13)$$

Below we present constraints on the dimensionful parameter  $\epsilon$ , which we label as  $p_{\text{ann}}$  in Table II for ease

of comparison with the constant  $p_{\text{ann}}$  case and general familiarity with that variable. To obtain a constraint on  $\langle\sigma v\rangle/M_\chi$  for a specific DM model, the bound on  $p_{\text{ann}}$  should be divided by  $f_{\text{eff,new}}$  for that model since

$$p_{\text{ann}} = f_{\text{eff,new}} \frac{\langle\sigma v\rangle}{M_\chi}. \quad (14)$$

[By definition, if  $f_{\text{sys}}(z) = e(z)$ , then  $f_{\text{eff,new}} = 1$ ; the derived constraint on  $p_{\text{ann}}$  is exactly the constraint on  $\langle\sigma v\rangle/M_\chi$  for such a model.] We have verified that this prescription accurately reproduces the constraints presented for individual leptonic annihilation channels in Ref. [8]. The fact that the  $f_{\text{sys}}(z)$  curves are generally lower than the original  $f(z)$  curves is reflected in lower  $f_{\text{eff,new}}$  values and hence weaker constraints on  $\langle\sigma v\rangle/M_\chi$ .

In Table III, we provide both the  $f_{\text{eff,new}}$  values computed using our new  $f_{\text{sys}}(z)$  curves and the  $f_{\text{eff}}$  values computed using the old  $f(z)$  curves from Ref. [3] but using the correct Fisher-matrix weighting described in the previous paragraph (these values were computed in an online supplement to Ref. [5], but the dot product was not properly weighted by the Fisher matrix, leading to few-percent deviations).

### B. Leverage in $\ell$ space of dark matter limits

The primary effects of dark matter annihilation on the CMB power spectra are an attenuation of power in both temperature and polarization especially at high  $l$ , an enhancement of low- $l$  polarization power, and low- $l$  polarization peak shifts. Since a number of cosmological parameters result in an attenuation of power at high  $l$  (e.g.,  $n_s$ ), one would expect most of the constraining leverage on dark

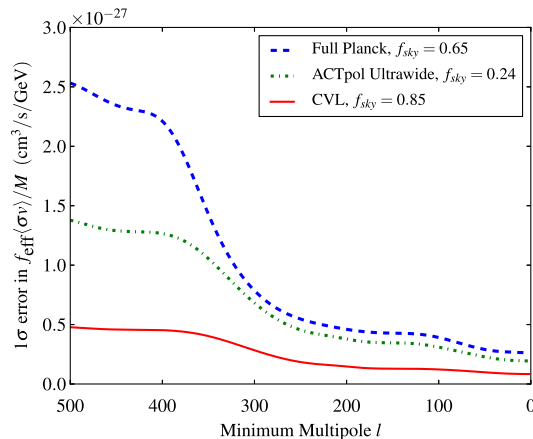


FIG. 2 (color online). Fisher projected constraint obtained by including the range  $500 < l < 5000$  and extending it cumulatively for each multipole below  $l = 500$ . Experimental parameters are from Planck, an ACTpol-like experiment, and a cosmic variance limited experiment (see Table I). Most of the leverage comes from  $250 < l < 400$ .

TABLE I. Experimental parameters used in forecasts.

Experiment	Beam FWHM (arcmin)	$10^6 \Delta T/T$ (I)	$10^6 \Delta T/T$ (Q,U)	$f_{\text{sky}}$
Planck <sup>a</sup>	7.1	2.2	4.2	0.65
ACTpol Ultrawide <sup>b</sup>	1.4	4.5	6.3	0.24
CMB Stage 4	3.0	0.1	0.1	0.50
Future high $l$	1.4	0.1	0.1	0.85

<sup>a</sup>Noise values are indicated per beam full width at half maximum (FWHM).

<sup>b</sup>We note that this represents just one possible configuration of the ACTpol survey.

matter limits to come from the low- $l$  TE and EE spectra, which break parameter degeneracies. To demonstrate the importance of low- $l$  polarization on improving constraints, we use Fisher forecasts to project the constraints obtainable by cumulatively adding the contribution to the Fisher matrix from each multipole below  $l = 500$  to the contribution from the range  $500 < l < 5000$ . We use experimental parameters typical of Planck [25], a current generation polarization experiment like ACTpol, and a cosmic variance limited experiment (see Table I). Including polarization information in the  $100 < l < 500$  range improves the constraint by a factor of  $\sim 3$  for ACTpol and  $\sim 5$  for Planck (see Fig. 2).

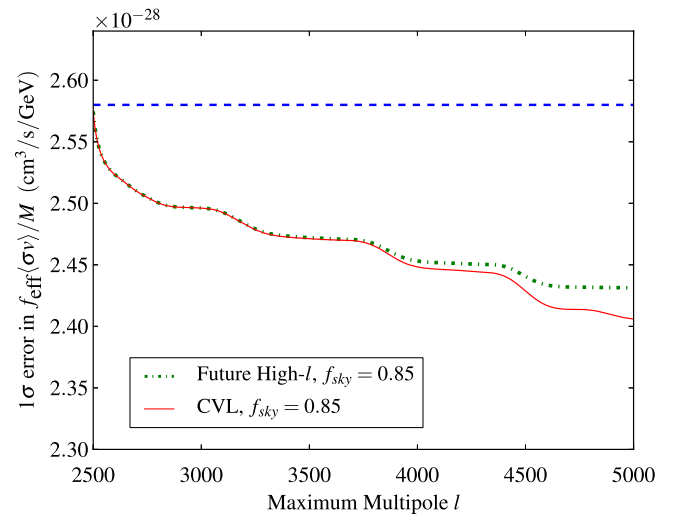


FIG. 3 (color online). Fisher projected constraints including the complete Planck data from  $2 < l < 2500$  (temperature and polarization) and extending it cumulatively for each multipole above  $l = 2500$  up to  $l = 5000$ . Experimental parameters are from a future high- $l$  experiment and a cosmic variance limited experiment. The dashed line shows the Fisher projection for the full Planck temperature and polarization release (up to  $l = 2500$ ). The improvements over Planck are 6% and 8% respectively, including all  $l$ 's up to 5000.

TABLE II. Upper limits at 95% C.L. for  $p_{\text{ann}}$  combining various data sets. The first column provides constraints when  $p_{\text{ann}}$  is assumed to be constant with redshift. The second and third columns assume redshift-dependent energy deposition based on the universal curve discussed in Sec. II A. The second column uses the original universal  $e(z)$  curve derived in Ref. [5]; the third column uses an updated curve that incorporates systematic corrections discussed in Ref. [8].

Data set	Constant annihilation	Nonconstant annihilation	Updated Nonconst. ( $\text{m}^3 \text{s}^{-1} \text{kg}^{-1}$ )
WMAP9	$p_{\text{ann}} < 1.20 \times 10^{-6}$	$p_{\text{ann}} < 1.26 \times 10^{-6}$	$p_{\text{ann}} < 1.21 \times 10^{-6}$
WMAP9 + Planck	$p_{\text{ann}} < 0.87 \times 10^{-6}$	$p_{\text{ann}} < 0.85 \times 10^{-6}$	$p_{\text{ann}} < 0.80 \times 10^{-6}$
WMAP9 + Planck + Planck lensing	$p_{\text{ann}} < 0.85 \times 10^{-6}$	$p_{\text{ann}} < 0.86 \times 10^{-6}$	$p_{\text{ann}} < 0.79 \times 10^{-6}$
WMAP9 + Planck + Planck lensing + ACT + SPT	$p_{\text{ann}} < 0.75 \times 10^{-6}$	$p_{\text{ann}} < 0.75 \times 10^{-6}$	$p_{\text{ann}} < 0.73 \times 10^{-6}$
All CMB + BAO	$p_{\text{ann}} < 0.70 \times 10^{-6}$	$p_{\text{ann}} < 0.66 \times 10^{-6}$	$p_{\text{ann}} < 0.67 \times 10^{-6}$
All CMB + BAO + HST	$p_{\text{ann}} < 0.71 \times 10^{-6}$	$p_{\text{ann}} < 0.74 \times 10^{-6}$	$p_{\text{ann}} < 0.66 \times 10^{-6}$
All CMB + BAO + HST + supernova	$p_{\text{ann}} < 0.70 \times 10^{-6}$	$p_{\text{ann}} < 0.71 \times 10^{-6}$	$p_{\text{ann}} < 0.66 \times 10^{-6}$

In contrast, the constraint obtained from adding high- $l$  ( $l > 2500$ ) temperature and polarization spectra to the full Planck data (temperature and polarization,  $2 < l < 2500$ ) plateaus around  $l = 4000$  for a future high- $l$  experiment (see Table I), with no more than a 6% improvement over full Planck. There is only an 8% improvement over Planck for a cosmic variance limited experiment, including all  $l$ 's up to 5000 (see Fig. 3).

### III. CURRENT CONSTRAINTS

To obtain 95% upper limits on  $p_{\text{ann}} = f_{\text{eff}} \langle \sigma v \rangle / M_\chi$ , we modified the recombination code RECFAST to include additional terms for the evolution of the hydrogen ionization fraction and matter temperature, given in Eqs. (7) to (10). We performed a likelihood analysis on various data sets using the Markov Chain Monte Carlo code COSMOMC [26]. We sampled the space spanned by  $p_{\text{ann}}$  and the six cosmological parameters:  $\Omega_b h^2$ ,  $\Omega_c h^2$ ,  $100\theta_*$ ,  $\tau$ ,  $n_s$ , and  $\ln 10^{10} A_s$ .

Previous analyses using Planck data [27] used only a small part of the WMAP9 polarization power spectrum [28]. Incorporating a larger range of the TE power spectrum can improve the constraint by up to a factor of  $\sim 2.4$ , depending upon how much of the WMAP9 polarization spectrum is included. Using Fisher forecasts, we find that the strongest constraint is obtained by including the WMAP9 temperature (TT) + TE power spectrum from  $l = 2$  to  $l = 431$  and including the Planck TT spectrum for higher multipoles ( $432 < l < 2500$ ). We also include high- $l$  data—a combination of ACT 2008–2010 [29] and SPT 2011–2012 [30] observations, using their power spectra in the range  $2500 < l < 4500$ , which is included in the publicly available Planck likelihood [31]. Several low-redshift (non-CMB) data sets are also combined. These include baryon acoustic oscillation data (BAO) from BOSS DR9 [32], Hubble Space Telescope measurements of over 600 Cepheid variables (HST) [33], and supernovae type Ia data from the Union 2.1 compilation (SN) [34].

When combining CMB data sets, we do not account for the covariance between disjoint  $l$  ranges from different

experiments as we expect this to be negligible [27]. In using the Planck likelihood code, we removed the TT power spectrum contribution from  $l < 431$  by setting the relevant diagonal elements of the covariance matrix to effectively infinity ( $10^{10}$ ) and the off-diagonal elements to zero.<sup>1</sup>

The dark matter annihilation constraints thus obtained are listed in Table II. We checked for convergence of the chains using a Gelman–Rubin test statistic, ensuring that the corresponding  $R - 1$  fell below 0.01. We obtained three sets of constraints, one with constant  $p_{\text{ann}}$ , one with  $p_{\text{ann}}(z)$  proportional to the original universal  $e(z)$  curve (shown as the blue curve in Fig. 1) to account for a generic redshift dependence of the energy deposition, and one with  $p_{\text{ann}}(z)$  proportional to an updated universal  $e(z)$  curve that includes systematic corrections as detailed in Sec. II A. The constraints using the updated universal curve with systematic corrections are also shown in Fig. 5. In general, there is a small improvement in the constraints using the updated  $e(z)$  curve incorporating systematic corrections. As discussed above, this is not expected *a priori* from the Fisher matrix analysis using the CMB data only; it likely reflects some combination of the breakdown of the approximations in the Fisher matrix approach, differences between the data and the idealized  $\Lambda$ CDM baseline used for the Fisher analysis, the effect of including non-CMB data sets, and the few-percent uncertainty in the constraints due simply to scatter between CosmoMC runs.

The greatest improvement to the WMAP9-only constraint comes from adding the Planck TT spectrum ( $\sim 50\%$ ) as it particularly constrains the spectral index  $n_s$ , which is strongly degenerate with the annihilation parameter  $p_{\text{ann}}$  (see Fig. 4). The high- $l$  CMB and BAO data sets improve our constraints by 8% and 9%, respectively. Adding to this the HST and SN data does not considerably improve these limits.

<sup>1</sup>We note that there is a 2.49% calibration difference between the Planck and WMAP9 power spectra [27]. Since the origin of this offset is unclear, in this work we take each data set as given and do not adjust either.

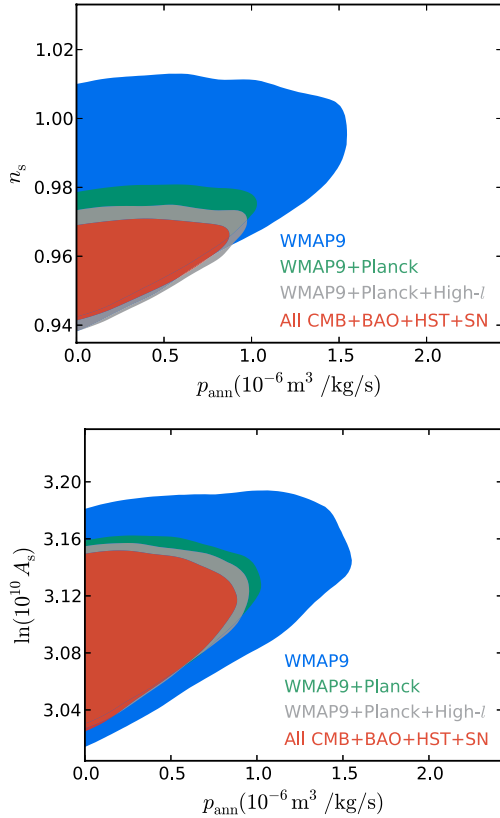


FIG. 4 (color online). 95% confidence limit contours for  $n_s$  vs  $p_{\text{ann}}$  and  $\ln(10^{10}A_s)$  vs  $p_{\text{ann}}$ , marginalized over the other parameters, for selected combinations of data sets.

#### IV. DISCUSSION

The constraint obtained from using the updated universal deposition curve and including all available data sets is a factor of  $\sim 2$  stronger than that from WMAP9 data alone [27]. The strongest constraint, including all available data, of  $p_{\text{ann}} < 0.66 \times 10^{-6} \text{ m}^3 \text{ s}^{-1} \text{ kg}^{-1}$  at 95% C.L., excludes annihilating dark matter of masses  $M_\chi < 26 \text{ GeV}$ , assuming a thermal cross section of  $3 \times 10^{-26} \text{ cm}^3 \text{ s}^{-1}$  and perfect absorption of injected energy ( $f_{\text{eff}} = 1$ ). Using a more realistic absorption efficiency of  $f_{\text{eff}} = 0.2$ , we exclude annihilating thermal dark matter of masses  $M_\chi < 5 \text{ GeV}$  at the  $2\sigma$  level.<sup>2</sup>

These constraints can be compared to dark matter models explaining a number of recent anomalous results from other indirect and direct dark matter searches. Recent measurements by the AMS-02 collaboration [35] confirm a rise in the cosmic ray positron fraction at energies above 10 GeV, which was found earlier by the PAMELA [36] and Fermi collaborations [37]. Such a rise is not easy to reconcile with known astrophysical processes, although contributions from Milky Way pulsars within  $\sim 1 \text{ kpc}$  of the Earth could

<sup>2</sup>This constraint on  $p_{\text{ann}}$  is a factor of 2 weaker than that found by Ref. [9], possibly due to the priors chosen in that work.

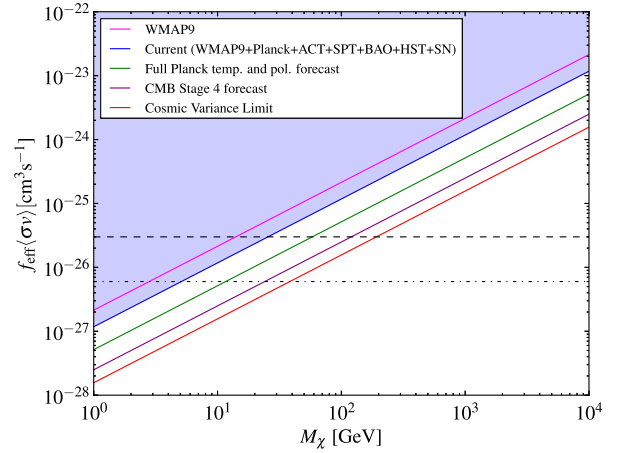


FIG. 5 (color online). From top to bottom: constraints on  $p_{\text{ann}}$  from WMAP9 alone (pink) and from current data including WMAP9, the Planck TT power spectrum and four-point lensing signal, ACT, SPT, BAO, HST, and SN data (blue). Also shown are Fisher forecasts for the complete Planck temperature and polarization power spectra (green), for a proposed CMB Stage IV experiment ( $50 < l < 4000$  combined with  $l < 50$  from Planck, shown in purple) and for a cosmic variance limited experiment (up to  $l = 4000$ ) (red). The dashed line shows the thermal cross section of  $3 \times 10^{-26} \text{ cm}^3 \text{ s}^{-1}$  for  $f_{\text{eff}} = 1$ . The dotted-dashed line shows the thermal cross section multiplied by a typical energy deposition fraction of  $f_{\text{eff}} = 0.2$  (see Table III).

provide a possible explanation [38–42]. Dark matter annihilating within the Galactic halo also remains a possible explanation of the positron excess [43–46]. Dark matter models considered in Ref. [44] to explain the AMS-02/PAMELA positron excess cannot have significant annihilation into Standard Model gauge bosons or quarks in order to be consistent with the antiproton-to-proton ratio measured by PAMELA, which is found to agree with expectations from known astrophysical sources [47]. In addition, the combination of the Fermi electron plus positron fraction [48,49] and the AMS-02/PAMELA positron excess suggest that a viable dark matter candidate would need to have a mass greater than  $\sim 1 \text{ TeV}$ . As found by Ref. [44], dark matter particles in the  $\sim 1.5 - 3 \text{ TeV}$  range with a cross section of  $\langle \sigma v \rangle \sim (6 - 23) \times 10^{-24} \text{ cm}^3/\text{s}$ , which annihilate into light intermediate states that in turn decay into muons and charged pions, can fit the Fermi, PAMELA, and AMS-02 data. Direct annihilations into leptons do not provide good fits [44]. Such high cross sections can be reconciled with the current dark matter abundance in the Universe in three ways: (i) Dark matter can have a thermal cross section at freeze-out, and the cross section can have a  $1/v$  dependence, called Sommerfeld enhancement [50,51]. If the cross section is Sommerfeld enhanced to be  $\sim 10^{-24}$  today in the Galactic halo, then it would be orders of magnitude larger at recombination



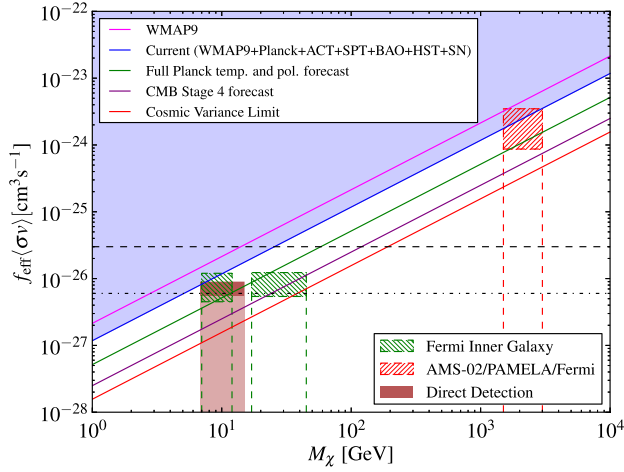


FIG. 6 (color online). Current constraints are compared with dark matter model fits to data from other indirect and direct dark matter searches. The data from indirect searches include those from AMS-02, PAMELA, and Fermi, and the data from direct searches include those from CDMS, CoGeNT, CRESST, and DAMA. The lighter shaded direct detection region allows for  $p$ -wave annihilations, and the dashed vertical lines for the indirect detection regions allow for  $p$ -wave annihilations for nonthermally produced dark matter.

(since  $v_{\text{recom}} < v_{\text{halo}}$ ). Such a possibility is strongly excluded by the CMB constraints (as noted in Ref. [3]) for a wide range of masses including those that fit the AMS-02 data. (ii) Dark matter has a thermal cross section at freeze-out, and Sommerfeld enhancement saturates at a cross section of  $\sim 10^{-24}$   $\text{cm}^3/\text{s}$ . So dark matter has this cross section just before (and during) recombination and also in the halo of the Milky Way. (iii) Dark matter particles are nonthermal, in which case the cross section has always been ( $\sim 10^{-24}$   $\text{cm}^3/\text{s}$ ). The last two possibilities are shown in Fig. 6 and are probed but not excluded by our current constraints. Here, we use the updated  $f_{\text{eff}}$  values from Table III corresponding to the best-fit annihilation channels found by Ref. [44].

One additional possibility is that dark matter has a  $p$ -wave annihilation cross section with a  $\sim v^2$  dependence on velocity. Dark matter that has a  $p$ -wave cross section and fits the AMS-02/PAMELA data would have to be non-thermal since the cross section during freeze-out would be orders of magnitude larger and would vastly overdeplete the relic density. Since  $v_{\text{recom}} \ll v_{\text{halo}}$ , the cross section around recombination can be orders of magnitude smaller in this case. We indicate this by dashed vertical lines in Fig. 6.

Recent direct detection experiments such as CDMS, CoGeNT, CRESST, and DAMA, have also reported anomalous signals that could potentially be interpreted as arising from dark matter [52–55]. For example, the CDMS collaboration recently reported three events above background where they expected only 0.7 events, by

TABLE III. Effective energy deposition fractions for 41 dark matter models. The third column is an updated version of Table I in Ref. [3], and the fourth column includes systematic corrections discussed in Sec. II A.

Channel	DM mass (GeV)	$f_{\text{eff}}$	$f_{\text{eff,new}}$
Electrons $\chi\chi \rightarrow e^+e^-$	1	0.85	0.45
	10	0.77	0.67
	100	0.60	0.46
	700	0.58	0.45
	1000	0.58	0.45
Muons $\chi\chi \rightarrow \mu^+\mu^-$	1	0.30	0.21
	10	0.29	0.23
	100	0.23	0.18
	250	0.21	0.16
	1000	0.20	0.16
	1500	0.20	0.16
Taus $\chi\chi \rightarrow \tau^+\tau^-$	200	0.19	0.15
	1000	0.19	0.15
XDM electrons $\chi\chi \rightarrow \phi\phi$ Followed by $\phi \rightarrow e^+e^-$	1	0.85	0.52
	10	0.81	0.67
	100	0.64	0.49
	150	0.61	0.47
XDM muons $\chi\chi \rightarrow \phi\phi$ Followed by $\phi \rightarrow \mu^+\mu^-$	1000	0.58	0.45
	10	0.30	0.21
	100	0.24	0.19
	400	0.21	0.17
XDM taus $\chi\chi \rightarrow \phi\phi, \phi \rightarrow \tau^+\tau^-$	1000	0.20	0.16
	2500	0.20	0.16
	200	0.19	0.15
	1000	0.18	0.14
XDM pions $\chi\chi \rightarrow \phi\phi$ Followed by $\phi \rightarrow \pi^+\pi^-$	100	0.20	0.16
	200	0.18	0.14
	1000	0.16	0.13
	1500	0.16	0.13
W bosons $\chi\chi \rightarrow W^+W^-$	2500	0.16	0.13
	200	0.26	0.19
	300	0.25	0.19
Z bosons $\chi\chi \rightarrow ZZ$	1000	0.24	0.19
	200	0.24	0.18
Higgs bosons $\chi\chi \rightarrow h\bar{h}$	1000	0.23	0.18
	200	0.30	0.22
b quarks $\chi\chi \rightarrow b\bar{b}$	1000	0.28	0.22
	200	0.31	0.23
Light quarks $\chi\chi \rightarrow u\bar{u}, d\bar{d}$ (50% each)	1000	0.28	0.22
	200	0.29	0.22

measuring nuclear recoils using silicon semiconductor detectors operating at 40 mK [53]. If the CDMS anomalous events are explained by dark matter, then they favor a best-fit dark matter mass of 8.6 GeV and a dark matter-nucleon cross section of  $1.9 \times 10^{-41}$   $\text{cm}^2$  (with 68% C.L. ranges of 6.5–15 GeV and  $2 \times 10^{-42} - 2 \times 10^{-40}$   $\text{cm}^2$ ) (see Fig. 4 in

Ref. [53]). The dark matter candidates that potentially explain the anomalous signals from the other direct detection experiments have best-fit regions that do not completely overlap in the two-dimensional mass/nucleon cross section space but have mass ranges that are comparable [53]. If we assume a thermal  $s$ -wave annihilation cross section during the recombination era and an  $f_{\text{eff}}$  from Table III corresponding to annihilation into  $b\bar{b}$ , the current constraints presented above start to probe, but do not exclude, such a dark matter candidate. However, future Planck results and those from a proposed CMB Stage IV experiment [56,57] will more definitively probe the relevant regime, as shown in Fig. 6. If dark matter has  $p$ -wave annihilations instead, then generic thermal dark matter can have annihilation cross sections at recombination orders of magnitude lower than the thermal cross section. This is indicated by a lighter-shaded direct detection region in Fig. 6.

Observations of the Galactic center and inner Galaxy by the Fermi gamma-ray telescope reveal an extended gamma-ray excess above known backgrounds, peaking at around 2–3 GeV. A population of unresolved millisecond pulsars has been proposed as a possible explanation, but as found by Ref. [58], in order for pulsars to reproduce the excess in the inner Galaxy, their luminosities and abundances would need to be quite different from any observed pulsar population. However, these measurements are well fit by dark matter particles with mass in the ranges 7–12 GeV (if annihilating mostly to leptons) and 25–45 GeV (if annihilating mostly to hadrons) and are consistent with a cross section of  $\sim 10^{-26}$  cm<sup>3</sup>/s [59–62]. For the higher mass range, we assume annihilations into quarks and gauge bosons and a thermal cross section. For the lower mass range, we assume annihilations into muons and taus and a thermal cross section. Figure 6 shows that we can probe but

not exclude this interpretation. The complete Planck data will better examine this possibility, as will data from the proposed CMB Stage IV experiment.

The constraints on the dark matter annihilation cross section and mass from the CMB are complementary and competitive with other indirect detection probes and offer a relatively clean way to measure dark matter properties in the early Universe. Current CMB experiments are starting to probe very interesting regions of dark matter parameter space, and future CMB polarization measurements have the potential to significantly expand the constrained regions or detect a dark matter signal.

## ACKNOWLEDGMENTS

The authors thank Erminia Calabrese and Silvia Galli for very useful correspondence and especially Renée Hlozek for help with the Planck likelihood. The authors also acknowledge helpful discussions with Alexander van Engelen, Rouven Essig, and Neal Weiner. M. M. is supported by an SBU-BNL Research Initiatives Seed Grant, Grant No. 37298, Project No. 1111593. This work is supported by the U.S. Department of Energy under cooperative research agreement Contract No. DE-FG02-05ER41360. The authors also gratefully acknowledge the use of the software packages CAMB and CosmoMC and the publicly available Planck and WMAP likelihoods. Some computations were performed on the General Purpose Cluster (GPC) supercomputer at the SciNet HPC Consortium. SciNet is funded by the Canada Foundation for Innovation under the auspices of Compute Canada, the Government of Ontario, Ontario Research Fund—Research Excellence, and the University of Toronto.

- 
- [1] N. Padmanabhan and D. P. Finkbeiner, *Phys. Rev. D* **72**, 023508 (2005).
  - [2] S. Galli, F. Iocco, G. Bertone, and A. Melchiorri, *Phys. Rev. D* **80**, 023505 (2009).
  - [3] T. R. Slatyer, N. Padmanabhan, and D. P. Finkbeiner, *Phys. Rev. D* **80**, 043526 (2009).
  - [4] S. Galli, F. Iocco, G. Bertone, and A. Melchiorri, *Phys. Rev. D* **84**, 027302 (2011).
  - [5] D. P. Finkbeiner, S. Galli, T. Lin, and T. R. Slatyer, *Phys. Rev. D* **85**, 043522 (2012).
  - [6] J. M. Cline and P. Scott, *J. Cosmol. Astropart. Phys.* **03** (2013) 044.
  - [7] R. Diamanti, L. Lopez-Honorez, O. Mena, S. Palomares-Ruiz, and A. C. Vincent, *J. Cosmol. Astropart. Phys.* **02** (2014) 017.
  - [8] S. Galli, T. R. Slatyer, M. Valdes, and F. Iocco, *Phys. Rev. D* **88**, 063502 (2013).
  - [9] L. Lopez-Honorez, O. Mena, S. Palomares-Ruiz, and A. C. Vincent, *J. Cosmol. Astropart. Phys.* **07** (2013) 046.
  - [10] C. Weniger, P. D. Serpico, F. Iocco, and G. Bertone, *Phys. Rev. D* **87**, 123008 (2013).
  - [11] A. Natarajan, *Phys. Rev. D* **85**, 083517 (2012).
  - [12] P. J. E. Peebles, *Astrophys. J.* **153**, 1 (1968).
  - [13] R. Bean, A. Melchiorri, and J. Silk, *Phys. Rev. D* **75**, 063505 (2007).
  - [14] S. Galli, R. Bean, A. Melchiorri, and J. Silk, *Phys. Rev. D* **78**, 063532 (2008).
  - [15] G. Hütsi, J. Chluba, A. Hektor, and M. Raidal, *Astron. Astrophys.* **535**, A26 (2011).

- [16] A. Natarajan and D. J. Schwarz, *Phys. Rev. D* **80**, 043529 (2009).
- [17] G. Giesen, J. Lesgourgues, B. Audren, and Y. Ali-Haïmoud, *J. Cosmol. Astropart. Phys.* **12** (2012) 008.
- [18] J. M. Shull and M. E. van Steenberg, *Astrophys. J.* **298**, 268 (1985).
- [19] X. Chen and M. Kamionkowski, *Phys. Rev. D* **70**, 043502 (2004).
- [20] M. Valdés and A. Ferrara, *Mon. Not. R. Astron. Soc.* **387**, L8 (2008).
- [21] S. R. Furlanetto and S. J. Stoeber, *Mon. Not. R. Astron. Soc.* **404**, 1869 (2010).
- [22] M. Valdés, C. Evoli, and A. Ferrara, *Mon. Not. R. Astron. Soc.* **404**, 1569 (2010).
- [23] C. Evoli, S. Pandolfi, and A. Ferrara, *Mon. Not. R. Astron. Soc.* **433**, 1736 (2013).
- [24] T. R. Slatyer, *Phys. Rev. D* **87**, 123513 (2013).
- [25] The Planck Collaboration, [arXiv:astro-ph/0604069](https://arxiv.org/abs/astro-ph/0604069).
- [26] A. Lewis and S. Bridle, *Phys. Rev. D* **66**, 103511 (2002).
- [27] P. A. R. Ade *et al.* (Planck Collaboration), [arXiv:1303.5076](https://arxiv.org/abs/1303.5076).
- [28] C. L. Bennett *et al.*, *Astrophys. J.* **208**, 20 (2013).
- [29] S. Das *et al.*, [arXiv:1301.1037](https://arxiv.org/abs/1301.1037).
- [30] K. K. Schaffer *et al.*, *Astrophys. J.* **743**, 90 (2011).
- [31] P. A. R. Ade *et al.* (Planck Collaboration), [arXiv:1303.5075](https://arxiv.org/abs/1303.5075).
- [32] K. S. Dawson *et al.*, *Astron. J.* **145**, 10 (2013).
- [33] A. G. Riess, L. Macri, S. Casertano, H. Lampeitl, H. C. Ferguson, A. V. Filippenko, S. W. Jha, W. Li, and R. Chornock, *Astrophys. J.* **730**, 119 (2011).
- [34] N. Suzuki *et al.*, *Astrophys. J.* **746**, 85 (2012).
- [35] M. Aguilar *et al.* (AMS Collaboration), *Phys. Rev. Lett.* **110**, 141102 (2013).
- [36] O. Adriani *et al.*, *Phys. Rev. Lett.* **111**, 081102 (2013).
- [37] M. Ackermann *et al.*, *Phys. Rev. Lett.* **108**, 011103 (2012).
- [38] D. Hooper, P. Blasi, and P. Dario Serpico, *J. Cosmol. Astropart. Phys.* **01** (2009) 025.
- [39] H. Yüksel, M. D. Kistler, and T. Stanev, *Phys. Rev. Lett.* **103**, 051101 (2009).
- [40] S. Profumo, *Central Eur. J. Phys.* **10**, 1 (2012).
- [41] D. Malyshev, I. Cholis, and J. Gelfand, *Phys. Rev. D* **80**, 063005 (2009).
- [42] D. Grasso *et al.*, *Astropart. Phys.* **32**, 140 (2009).
- [43] H.-B. Jin, Y.-L. Wu, and Y.-F. Zhou, *J. Cosmol. Astropart. Phys.* **11** (2013) 026.
- [44] I. Cholis and D. Hooper, *Phys. Rev. D* **88**, 023013 (2013).
- [45] L. Bergstrom, T. Bringmann, I. Cholis, D. Hooper, and C. Weniger, *Phys. Rev. Lett.* **111**, 171101 (2013).
- [46] J. Kopp, *Phys. Rev. D* **88**, 076013 (2013).
- [47] O. Adriani *et al.*, *Phys. Rev. Lett.* **105**, 121101 (2010).
- [48] A. A. Abdo *et al.*, *Phys. Rev. Lett.* **102**, 181101 (2009).
- [49] M. Ackermann *et al.*, *Phys. Rev. D* **82**, 092004 (2010).
- [50] M. Pospelov and A. Ritz, *Phys. Lett. B* **671**, 391 (2009).
- [51] N. Arkani-Hamed, D. P. Finkbeiner, T. R. Slatyer, and N. Weiner, *Phys. Rev. D* **79**, 015014 (2009).
- [52] R. Bernabei *et al.*, [arXiv:1301.6243](https://arxiv.org/abs/1301.6243).
- [53] R. Agnese *et al.* (CDMS Collaboration), *Phys. Rev. Lett.* **111**, 251301 (2013).
- [54] C. E. Aalseth *et al.*, *Phys. Rev. Lett.* **107**, 141301 (2011).
- [55] G. Angloher *et al.*, *Eur. Phys. J. C* **72**, 1 (2012).
- [56] K. N. Abazajian *et al.*, [arXiv:1309.5381](https://arxiv.org/abs/1309.5381).
- [57] K. N. Abazajian *et al.*, [arXiv:1309.5383](https://arxiv.org/abs/1309.5383).
- [58] D. Hooper, I. Cholis, T. Linden, J. Siegal-Gaskins, and T. Slatyer, *Phys. Rev. D* **88**, 083009 (2013).
- [59] D. Hooper and T. Linden, *Phys. Rev. D* **84**, 123005 (2011).
- [60] D. Hooper and L. Goodenough, *Phys. Lett. B* **697**, 412 (2011).
- [61] D. Hooper, C. Kelso, and F. S. Queiroz, *Astropart. Phys.* **46**, 55 (2013).
- [62] C. Gordon and O. Macias, *Phys. Rev. D* **88**, 083521 (2013).